

RESEARCH ARTICLE

10.1002/2016JA023780

Auroral precipitating energy during long magnetic storms

F. R. Cardoso¹ , M. V. Alves², G. K. Parks³ , M. O. Fillingim³ , F. J. R. Simões Junior⁴, E. Costa Junior⁵, and D. Koga² 

Key Points:

- Quasiperiodic energy flux enhancement during magnetic storms with long recovery phases
- The precipitating electron energy affects directly the auroral electrojets during long recovery phase events
- Long recovery phases in magnetic storms may be generated by the solar wind-magnetosphere directly driven mechanism

Correspondence to:

F. R. Cardoso,
flaviacardoso@usp.br

Citation:

Cardoso, F. R., M. V. Alves, G. K. Parks, M. O. Fillingim, F. J. R. Simões Junior, E. Costa Junior, and D. Koga (2017), Auroral precipitating energy during long magnetic storms, *J. Geophys. Res. Space Physics*, 122, doi:10.1002/2016JA023780.

Received 7 DEC 2016

Accepted 12 MAY 2017

Accepted article online 16 MAY 2017

¹Escola de Engenharia de Lorena, Universidade de São Paulo (EEL/USP), Lorena, Brazil, ²Instituto Nacional de Pesquisas Espaciais, São José dos Campos, São Paulo, Brazil, ³Space Science Laboratory, University of California, Berkeley, California, USA, ⁴Departamento de Física, Universidade Federal de Pelotas, Pelotas, Brazil, ⁵Campus Ouro Preto, Instituto Federal de Minas Gerais, Ouro Preto, Brazil

Abstract The power energy input carried by precipitating electrons into the auroral zone is an important parameter for understanding the solar wind-magnetosphere energy transfer processes and magnetic storms triggering. Some magnetic storms present a peculiar long recovery phase, lasting for many days or even weeks, which can be associated with the intense and long-duration auroral activity named HILDCAA (High Intensity Long Duration Continuous AE Activity). The auroral energy input during HILDCAAs has been pointed out as an essential key issue, although there have been very few quantitative studies on this topic. In the present work, we have estimated the auroral electron precipitating energy during the events of long (LRP) and short (SRP) storm recovery phase. The energy has been calculated from the images produced by the Ultraviolet Imager (UVI) on board the Polar satellite. In order to obtain accurate energy values, we developed a dayglow estimate method to remove solar contamination from the UVI images, before calculating the energy. We compared the UVI estimate to the Hemispheric Power (HP), to the empirical power obtained from the *AE* index, and to the solar wind input power. Our results showed that the UVI electron precipitating power for the LRP events presented a quasiperiodic fluctuation, which has been confirmed by the other estimates. We found that the LRP events are a consequence of a directly driven system, where there is no long-term energy storage in the magnetosphere, and the auroral electrojets during these events are directly affected by the electron precipitating power.

1. Introduction

The comprehension of the geomagnetic disturbances demands a deep qualitative and quantitative study of the energy causing and driving the events. Solar wind parameters have been largely used as an attempt to obtain energy estimates available for the magnetospheric dynamics [Akasofu, 1981; Gonzalez, 1990]. The solar wind energy input is mainly dissipated as Joule heating in the ionosphere, ring current injection, and particle precipitation [Koskinen and Tanskanen, 2002]. Although the ring current has been considered the largest energy sink within the magnetosphere [Akasofu, 1981], Palmroth *et al.* [2006] pointed out that the present understanding is that the total energy during magnetic storms is roughly equally divided between the ionosphere and the ring current.

Akasofu [1981] introduced the ϵ parameter which describes the energy transfer from the solar wind into the magnetosphere. Gonzalez [1990] reviewed a large number of the solar wind-magnetosphere coupling functions and commented that all the widely used equations for the energy transfer are related to the dawn-dusk component of the solar wind electric field given by the product of the solar wind speed (v) and the southward component of the interplanetary magnetic field IMF (B_s) and to the energy transfer at the magnetopause due to large-scale reconnection [Koskinen and Tanskanen, 2002].

The solar wind energy input may be responsible for triggering magnetic storms and substorms. Some magnetic storms present a peculiar long recovery phase which can last for many days or even weeks. Intense and long-duration auroral activity has been observed during the long-lasting recovery phase, which Tsurutani and Gonzalez [1987] has named High Intensity Long Duration Continuous AE Activity or simply HILDCAA. The long recovery phase during the magnetic storm has been attributed to the fact that the ring current takes more time to return to prestorm conditions.

The magnetospheric energy dissipation can be derived empirically from ground-based measurements, particularly from the geomagnetic indices. *Akasofu* [1981] and *Ahn et al.* [1983] showed that the precipitating particle power varies in harmony with the *AE* index and proposed a simple linear relation between them. However, using geomagnetic indices and space instrument data, *Ostgaard et al.* [2002] pointed out that we should not expect a linear relation between the electron energy deposition and the geomagnetic indices. Based on the X-ray imager PIXIE and the Ultraviolet Imager (UVI), they obtained a nonlinear relation under the assumption that the *AE* index is due to ionospheric Hall currents and the polar cap potential slightly saturates for large *AE* values.

The auroral emission is a good monitor of the near-Earth magnetospheric processes, since the polar region is very sensitive to the effects of magnetosphere-ionosphere coupling. The auroral activities have been mostly studied during substorms, which tend to occur on the nightside of the auroral region [e.g., *Fillingim et al.*, 2000, 2001, 2005; *Chua et al.*, 2004]. This nightside occurrence avoids the sunlight contamination, which is named dayglow, in the auroral emission [*Meier*, 1991]. There are some known dayglow removal techniques applied to the auroral emission estimate, e.g., the methods of *Lummerzheim et al.* [1997], *Germany et al.* [1998], and *Liou et al.* [2001].

The particle precipitation in the polar region and the generated auroral emission may be good parameters to study HILDCAAs, since these events are related to the intense and long-lasting auroral activity. Moreover, *Hajra et al.* [2014] claimed that there have been very few quantitative studies on the HILDCAA energy budget. In the present work, we have estimated the precipitating auroral electron energy during the events of long and short magnetic storm recovery phase. We have selected three magnetic storms associated with HILDCAAs and three ordinary magnetic storms. The long recovery phase (LRP) events are related to HILDCAAs. The short recovery phase (SRP) occurs during ordinary magnetic storms.

The auroral energy deposition has been estimated over the entire auroral region, including the dayside, using auroral images from the Polar UVI instrument. The UVI is a small sophisticated camera with a two-dimensional intensified-CCD detector, on board the Polar spacecraft, which permits the energy deposited by electron precipitation in the auroral region to be estimated [*Torr et al.*, 1995]. The loss processes in the LBH (Lyman Birge Hopfield) long auroral emission (LBHL) are negligible and the brightness in this wavelength range (1600–1800 Å) is directly proportional to the electron precipitating energy [*Germany et al.*, 1990, 1994; *Torr et al.*, 1995].

Palmroth et al. [2006] compared the three mentioned dayglow removal methods of *Lummerzheim et al.* [1997], *Germany et al.* [1998], and *Liou et al.* [2001] and observed that they disagree significantly on the auroral power estimate during geomagnetic events. Such a result has been attributed to the differences on the conversion from photon brightness to the total power and on the accuracy of determining the dayglow quantity mixed with the auroral emission. To obtain accurate energy values, we developed a dayglow estimate method, carefully selecting dayglow brightness with no auroral emission. We remove the solar contamination from the UVI images before computing the auroral energy. The UVI power is also compared to other power estimates, as explained next.

This paper is organized as follows. We have described the UVI instrument and the images in section 2 and the dayglow estimate method, which was developed and used in this work, in section 3. Our results are shown in section 4, presented in three parts. First, in section 4.1, we show and discuss the UVI precipitating auroral electron energy estimated for SRP and LRP events and we also compare it to the Hemispheric Power (HP). Second, in section 4.2, the power dissipated in the auroral region has been estimated from the *AE* index and compared to the UVI power during the events. Third, the solar wind input power has been calculated and compared to the UVI precipitating power in section 4.3. Finally, our concluding remarks are presented in section 5.

2. The UVI Images

The UVI instrument generates a two-dimensional image which is an array of 224 by 200 pixels for each time instant, at every 30 s. These dimensions correspond to the two perpendicular diameters of the UVI circular field of view, yielding a per pixel spatial resolution of 0.036° in one direction and 0.04° in the other direction. Figure 1 displays examples of the UVI images and the details are explained in section 3.

The UVI operates in the far ultraviolet, over a wavelength range from 1300 to 1900 Å, having a filter wheel to select one of the five available far ultraviolet spectral regions for imaging. One of the filters can be adjusted for N_2 LBHL, which has a passband around 170 nm, and where there is almost no loss processes present.

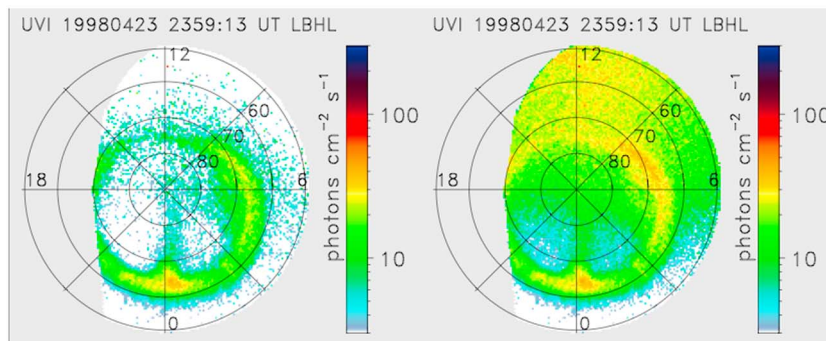


Figure 1. UVI image displaying (left) auroral emission, since the dayglow has been removed by the method described in section 3; (right) the dayglow, as an intense yellow region mostly on the dayside, seen concurrently with the auroral emission. The UVI image uses magnetic coordinates.

Shorter LBH (LBHs) wavelengths still lie in the range of the O_2 absorption and may vary with the energy of the injected particles. LBH emission is only slightly attenuated on its path and the intensity is directly proportional to the auroral energy flux injected by particle precipitation into the atmosphere [Torr et al., 1995; Germany et al., 1990, 1998].

The instrument view angle changes during the orbit time, and the apparent emission brightness can change as well. The LOS (line of sight) emission intensity increases with the instrument look angle due to the enlargement of the optical path length through a given column-integrated emission layer [Germany et al., 1998]. The UVI LBH images have to be corrected by the LOS geometry factor. This correction changes the image for a nadir view perspective (null look angle), placing the spacecraft position to the end of a vertical line (local zenith) passing through the emission point.

The imager is mounted on a pointable despun platform permitting continuous auroral imaging and is capable of measuring features under both sunlit and nightside conditions simultaneously [Torr et al., 1995]. Although the UVI instrument was designed to reduce the dayglow in the data, there is still solar contamination in the images. Before computing the auroral energy, the dayglow must be removed. We have thus developed a dayglow estimate method to remove solar contamination from the UVI images.

3. The Dayglow Estimate Method

The dayglow observed in the UVI images is generated by photoelectrons produced by solar extreme ultraviolet radiation and scattered solar UV (ultraviolet) photons [Torr et al., 1995]. Figure 1 shows two images obtained by the UVI instrument at the same time instant. The dayglow, concurrently with the auroral emission, can be

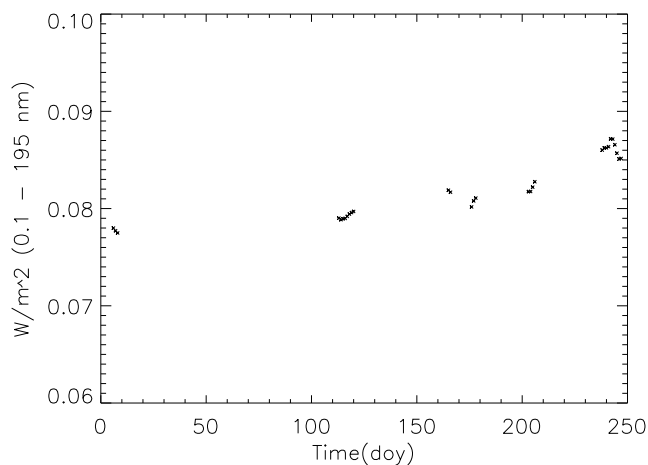


Figure 2. Solar vacuum ultraviolet daily average integrated over 0.1 to 195 nm during the events using FISM (Flare Irradiance Spectral Model) [Chamberlin et al., 2007, 2008].

observed on Figure 1 (right) as an intense yellow region mostly on the dayside. Figure 1 (left) contains basically auroral light emission, since the dayglow has been removed using the dayglow estimate method developed in this work and described next.

Assuming that pixels with the same solar zenith angle (χ_{sza}) contribute with the same amount of dayglow intensity, we are able to remove the undesirable dayglow from the UVI images [Lummerzheim et al., 1997; Liou et al., 2001]. The solar zenith angle is defined between the pixel-Sun line and the local zenith. The pixels at the UVI image are binned by χ_{sza} . The dayglow intensity as a function of the χ_{sza} was computed

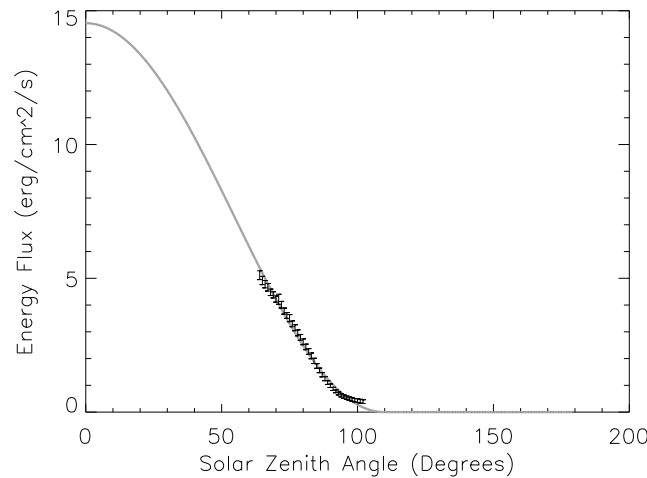


Figure 3. Black dots with error bars represent the dayglow energy flux obtained from the UVI images for the solar zenith angle range from 64 to 102°. Gray curve corresponds to the extrapolated dayglow UVI estimate, covering from 0 to 180°, using the method described in section 3.

by averaging the energy for each χ_{sza} bin, as performed by Lummerzheim *et al.* [1997]. However, Lummerzheim *et al.* [1997] excluded pixels within the auroral oval due to the auroral activity presence, while we carefully selected the UVI images during no active times, with no auroral emission.

We selected a set of 1308 UVI images under quiet conditions within the year of 1998, when the UVI was imaging the north hemisphere. The quiet day dayglow data and the events we analyzed were collected within the same year, in order to avoid the dayglow emission variability caused by the solar activity changing with the 11 year solar cycle. We estimated the daily values of the solar vacuum ultraviolet (UV) irradiance integrated over 0.1 to 195 nm

during the events, using FISM (Flare Irradiance Spectral Model) [Chamberlin *et al.*, 2007, 2008], as presented in Figure 2. The solar UV varies between the narrow range of 0.077 and 0.087 W/m² during the events. The dayglow method developed here may be applied to similar solar UV range conditions.

Even though our data set included a reasonable number of the UVI images, there is still a lack of the dayglow estimate for lower and higher χ_{sza} values. These pixels are located in the lower latitudes where the instrument rarely images. The errors related to the dayglow average computing are large for these χ_{sza} values due to the reduced number of pixels in the bins. In order to minimize the errors, only groups with the number of pixels greater than 75% of the most “populated” bin were considered. Hence, the UVI dayglow energy flux estimate came out within a limited small χ_{sza} range, from 64 to 102°. The black dots with error bars in Figure 3 represent the obtained dayglow energy flux versus solar zenith angle obtained from the UVI images. The error bars are small and represent the standard deviation calculated from the square root of the variance in the UVI dayglow data for each solar zenith angle bin. The error bars are larger for lower χ_{sza} , but proportionately smaller, reaching 3 to 5% (about 0.188 ergs/cm²/s) of the dayglow energy for the χ_{sza} covering from 64 to 87°, 6 to 10 % (about 0.069 ergs/cm²/s) for 88 to 95°, and 11 to 17% (about 0.060 ergs/cm²/s) for 96 to 102°. The error may be significant for large χ_{sza} where there are small values of dayglow energy.

We used an empirical function to extrapolate the dayglow energy estimate for the $\chi_{sza} < 64$ and $> 102^\circ$. This procedure permits estimating accurately the dayglow energy flux for an extended χ_{sza} range, $0 < \chi_{sza} < 180$. The empirical equation for the dayglow energy flux (D_G) is given by [Germany *et al.*, 1990]:

$$D_G = A \cos^2(\phi \chi_{sza}), \tag{1}$$

where A is the amplitude, ϕ and χ_{sza} are the angles. The parameters A and ϕ in equation (1) were determined as 53 ergs/cm²/s and 0.82 for the best fit with the dayglow energy flux estimated from the UVI data (black dots with error bars in Figure 3). The A and ϕ values may not change significantly during the events, since the solar UV varies between a narrow range of 0.01 W/m², as presented in Figure 2. The A parameter is an adjustment due to the solar activity variation; χ_{sza} angle is calculated for the pixel located on the surface of the Earth; the angle ϕ is an adjustment to χ_{sza} due to the fact that the pixel source is in the atmosphere, above the surface of the Earth. The final dayglow energy flux estimate, from the UVI images plus extrapolation, for all χ_{sza} values from 0 to 180° is shown in Figure 3 as a gray curve.

We used the dayglow estimate as a function of the χ_{sza} to subtract the solar contamination from the UVI images. Once the solar contamination is removed, we are left with the precipitating auroral electron energy, as shown in Figure 1 (left), where the UVI image contains almost only auroral emission.

Table 1. Characteristics of the Events

| SRP Events (Ordinary Magnetic Storms) | | | |
|---------------------------------------|-------------------------------|-------------------------|--------------------|
| Event | Date | Recovery Phase Duration | <i>Dst</i> Minimum |
| 1 | 6–8 January 1998 | 1.25 days | –77 nT |
| 2 | 14–15 June 1998 | 1.08 days | –55 nT |
| 3 | 25–27 June 1998 | 1.50 days | –101 nT |
| LRP Events (HILDCAAs) | | | |
| 4 | 23–30 April 1998 | 6.13 days | –69 nT |
| 5 | 22–29 July 1998 | 5.00 days | –48 nT |
| 6 | 26 August to 3 September 1998 | 7.17 days | –158 nT |

4. Results and Discussion

Our results show the precipitating auroral electron energy estimated from the UVI images during short and long magnetic storm events and a comparison to other energy computing parameters. In section 4.1, we present the UVI energy and the Hemispheric Power, which is the auroral power input obtained from instruments on board the NOAA Polar-Orbiting Operational Environmental Satellite (POES). The auroral power dissipation is obtained empirically from the *AE* geomagnetic index and is compared to the UVI power in section 4.2. The solar wind energy input is shown in section 4.3.

We selected six events of magnetic storms. The date of the events, the duration of their recovery phases, and the minimum of the *Dst* index are displayed in Table 1. The Events 1–3 in Table 1 exhibit short recovery phases, lasting less than 2 days. We call these ordinary magnetic storm SRP (short recovery phase) events, as already mentioned.

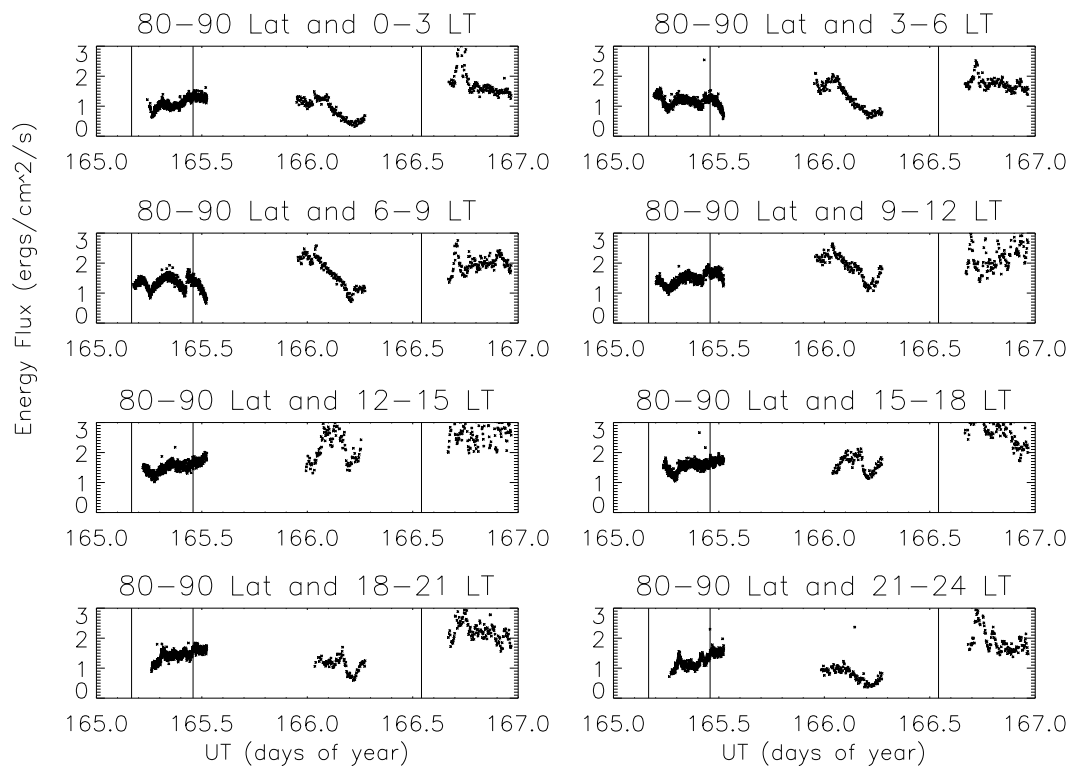


Figure 4. Energy flux time evolution computed over the area of 80 to 90° ML and 3 h MLT for the SRP event in 14–16 June 1998 (Event 2). The plots in this paper are marked with vertical lines which indicate the magnetic storm phases: the first vertical line points out the beginning of the main phase; the second line, the beginning of the recovery phase, and the third one, the end of the recovery phase.

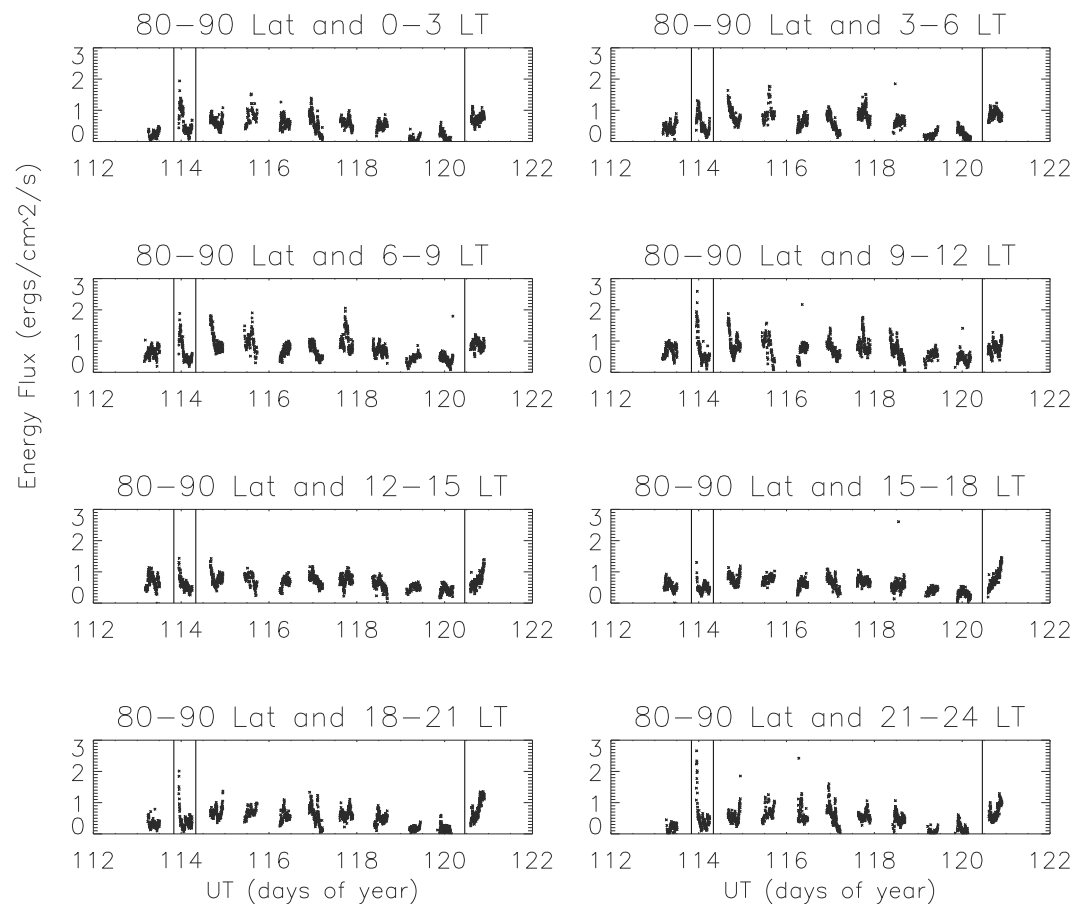


Figure 5. Energy flux time evolution computed over the area of 80 to 90° ML and 3 h MLT for the LRP event of 23–30 April 1998 (Event 4).

The Events 4–6 present long recovery phases lasting more than 2 days. The requirement of the 2 day duration is taken from the definition of a HILDCAA phenomenon, which are (1) *high intensity*, the AE index peak must be higher than 1000 nT during the event; (2) *long duration*, high and continuous AE activity must last for at least 2 days; (3) *continuous AE activity*, AE index value must not fall below 200 nT for intervals longer than 2 h at a time; (4) the event must occur outside the main phase of a geomagnetic storm [Tsurutani and Gonzalez, 1987]. The Events 4 and 5 in Table 1 apply to all the previous four criteria as verified by Guarnieri et al. [2007]. The Event 6 complies with the criteria 1, 2, and 4, since the AE index peaks at about 1600 nT and there is high and continuous AE activity outside of the storm main phase. The criterion 3 seems to be followed at least for the first half of the recovery phase, but we have not strictly verified it. We call the three magnetic storms associated with HILDCAAs LRP (long recovery phase) events, as mentioned previously.

4.1. UVI Estimate and Hemispheric Power

The energy deposition by precipitating electrons in the auroral zone has been quantitatively estimated from the UVI images. Before computing the energy, the images have been properly treated. We applied the spacecraft LOS correction, explained in section 2, to the LBHI images. Next, we removed the solar contamination from the UVI images using the dayglow estimate method described in section 3.

The UVI field of view constantly changes as the spacecraft moves. The Polar spacecraft takes about 18 h to complete a highly eccentric 9.0 by 1.8 R_E orbit and the auroral oval is covered globally only for distances greater than about 6 R_E , roughly 9 h, assuming that the equatorward auroral oval boundary is near 60° ML (magnetic latitude) [Torr et al., 1995]. Thus, the area over which the energy is integrated may be an important parameter to obtain an accurate estimate of the energy transferring into the auroral zone.

We have calculated the energy flux for each area of 10° ML and 3 h MLT (Magnetic Local Time) in the UVI images to maintain the area constant during the time interval of the estimate. Only completed covered sectors

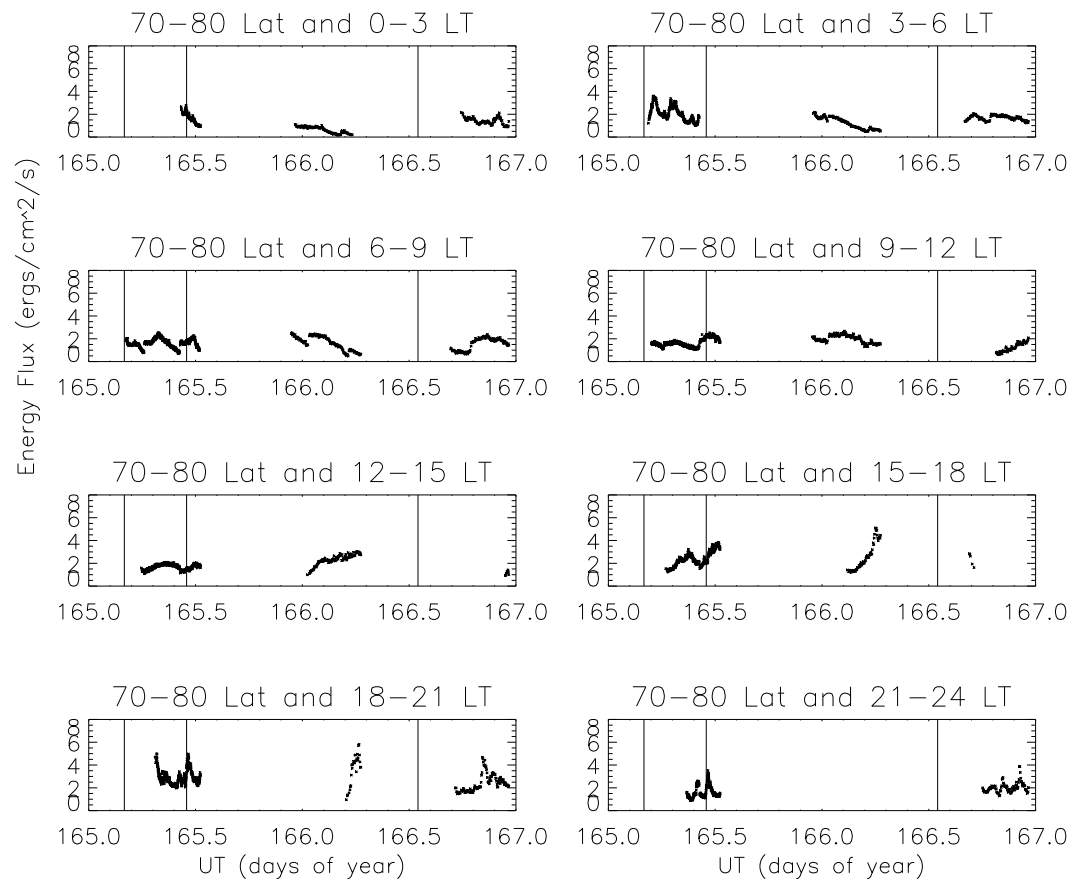


Figure 6. Energy flux time evolution computed over the area of 70 to 80° ML and 3 h MLT for the SRP event in 14–16 June 1998 (Event 2).

of 10° ML and 3 h MLT have been considered. The auroral region was assumed to extend from 50° to 90° ML for 0 to 24 MLT. However, we do not display the energy flux for 50° to 60° ML and for 60° to 70° ML due to the large lack of data in both of these latitude ranges.

Figures 4 to 7 show the energy flux computed for each magnetic local time sector during the SRP in 14–16 June 1998, and the LRP in 23–30 April 1998, which correspond to Events 2 and 4 in Table 1. We only display two events because the groups of SRP and LRP present similar characteristics. The panels show the time evolution of the energy flux calculated for each sector. The vertical lines in the plots correspond to the magnetic storm phases: the first vertical line points out the beginning of the main phase after the positive *Dst* peak; the second line at the maximum *Dst* negative peak, and the third one, the end of the recovery phase at the return to prestorm *Dst* values.

Comparing the SRP (Figures 4 and 6) and the LRP events (Figures 5 and 7), we observe a quasiperiodic energy flux enhancement in the LRP energy flux at all sectors. At the 80° to 90° ML, there are similarities along the MLT for the LRP and the energy flux is higher in the dayside for the SRP events. At the 70° to 80° ML, the energy flux seems higher at the nightside and near dusk for both events, but it reaches larger values for the LRP, about 7 ergs/cm²/s, and 5 ergs/cm²/s for the SRP event (Figures 6 and 7). Although there is a small amount of data for the SRP event at 60° to 70° ML, the energy flux reaches about 10 ergs/cm²/s for the SRP and 20 ergs/cm²/s for the LRP (not shown here).

Once the energy flux for small and constant areas (Figures 4 to 7) has been analyzed, we then look at the global behavior of the auroral power. We calculated the power from the UVI images for the total auroral area within the instrument field of view. However, as the area constantly changes, we required the aurora region area in the energy flux estimate to be over 60%. This procedure minimizes the disadvantage that the varying area may affect the power estimate, and we estimated the time evolution of the UVI total power for the SRP and LRP events.

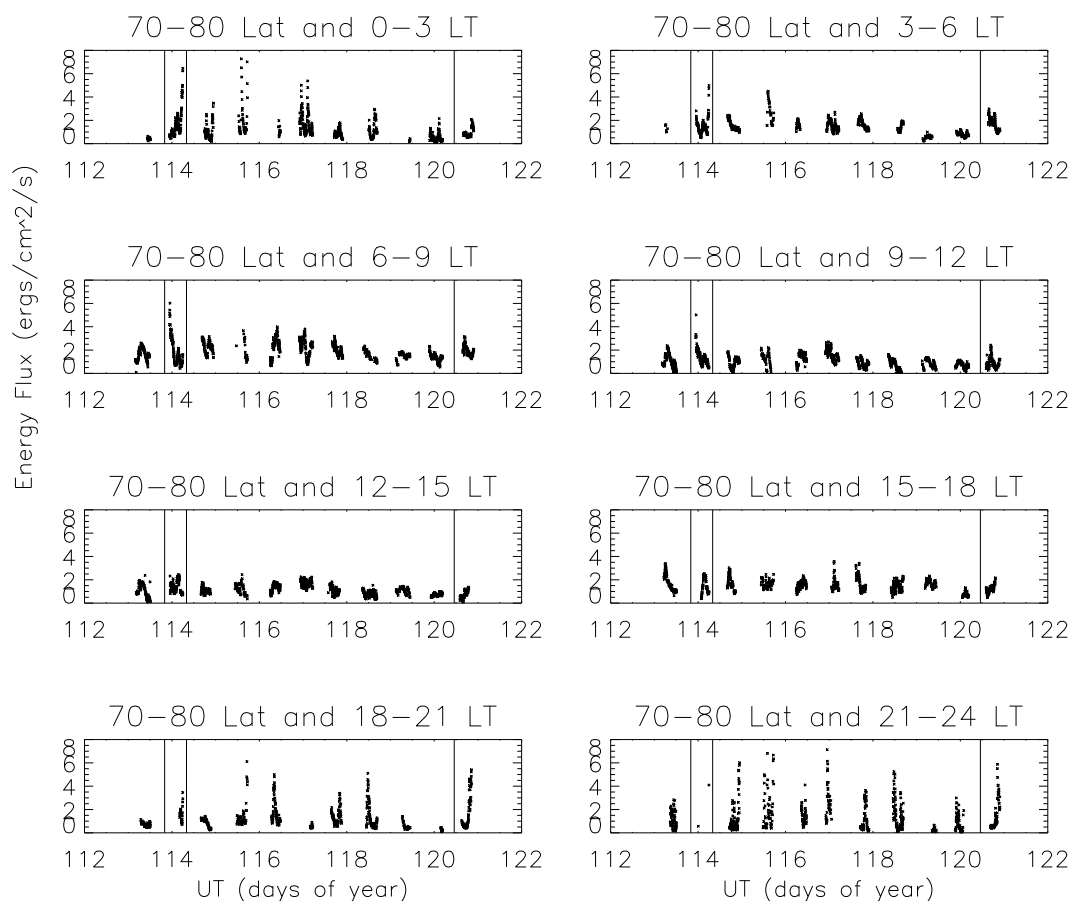


Figure 7. Energy flux time evolution computed over the area of 70 to 80° ML and 3 h MLT for the LRP event of 23–30 April 1998 (Event 4).

The UVI total power is shown as black triangles in Figures 8 to 10 for the SRP events and in Figures 11 to 13 for the LRP events. The absence of data is represented by blanks. Comparing the events, we can notice that the power for the LRP events presents higher values and a quasiperiodic variation, similar to the energy flux for sectors observed in Figures 5 and 7. The sectors of 70° to 80° ML (Figures 6 and 7) contribute most to the total UVI power for LRP and for SRP events.

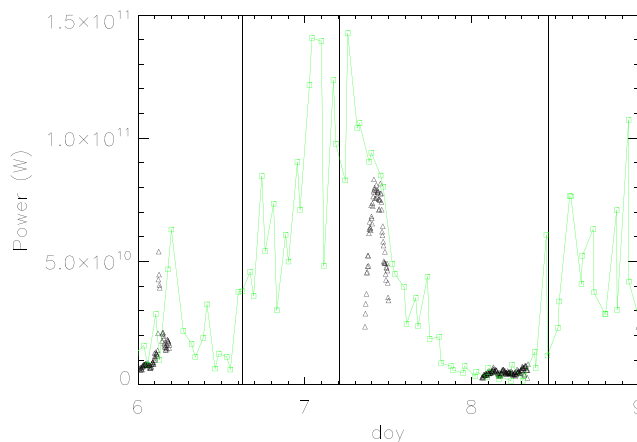


Figure 8. The UVI total power over the entire polar region from 50° to 90° (black triangles) and the HP (green squares) during the SRP event of 6–8 January 1998, Event 1.

We have compared the UVI total power to the Hemispheric Power [Emery *et al.*, 2006, 2008]. The power flux observations obtained during a single pass of the satellite NOAA POES over the polar region during 25 min are used to estimate the total power. The HP is estimated along the satellite track extrapolated for the entire auroral oval through statistical precipitation patterns. The measurements performed since NOAA-12 in 1991 are used to correct the estimate by taking into account how the satellite passes over a statistical auroral oval. From Table 1 in Emery *et al.* [2008],

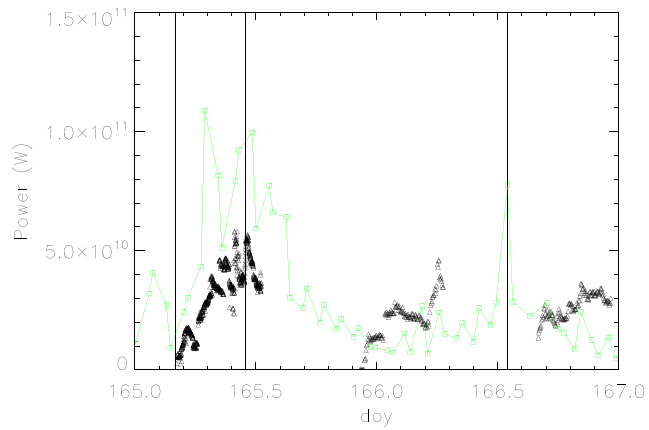


Figure 9. UVI total power over the entire polar region from 50° to 90° (black triangles) and the HP (green squares) during the SRP event of 14–16 June 1998, Event 2.

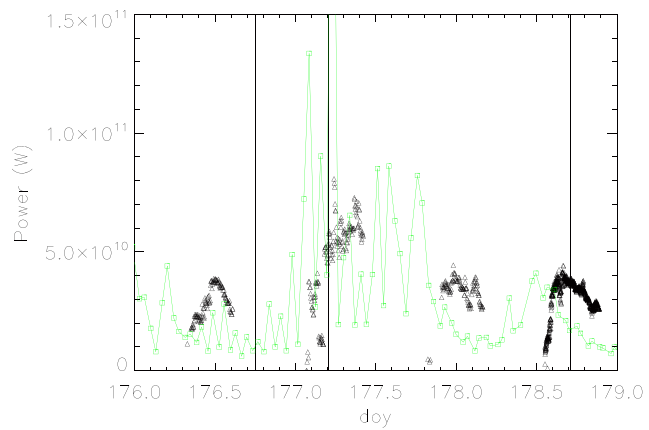


Figure 10. UVI total power over the entire polar region from 50° to 90° (black triangles) and the HP (green squares) during the SRP event of 25–27 June 1998, Event 3.

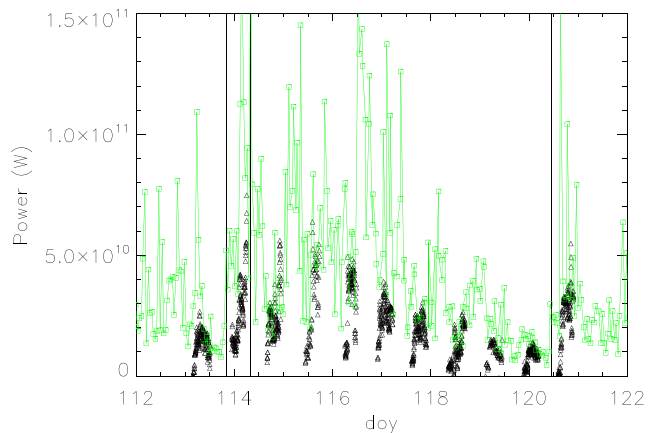


Figure 11. UVI total power over the entire polar region from 50° to 90° (black triangles) and the HP (green squares) during the LRP event of 23–30 April 1998, Event 4.

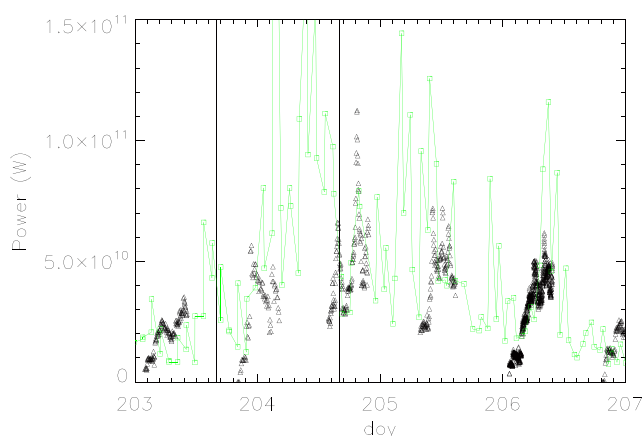


Figure 12. UVI total power over the entire polar region from 50° to 90° (black triangles) and the HP (green squares) during the LRP event of 22–29 July 1998, Event 5.

the NOAA-12 estimates that are the base of NOAA POES HP estimates starting in 1991 after a gap at the end of NOAA-10 observations, could be about 75% higher than the previous NOAA TIROS-based HP estimates from 1978 to 1991 or the DMSP HP estimates. However, Figures 8 to 13 show the NOAA HP estimates to be comparable to the UVI estimates except for Event 4 in Figure 11.

The HP is presented in Figures 8 to 13 as green lines connecting squares. We may notice that the HP roughly follows the UVI power behavior (black triangles) and clearly confirms the quasiperiodic variation seen in the UVI total power for the LRP events. The power peaks roughly around the *Dst* minimum (close to the second vertical line in Figures 8 to 13) for the UVI and for the HP estimate.

4.2. UVI Estimate and AE Index Empirical Power

The energy deposition by auroral precipitating electrons can be estimated not only from spaceborne instruments but also by ground measurements. The auroral energy dissipation can be obtained empirically from the geomagnetic indices. *Akasofu* [1981] proposed a linear relation between the precipitating particle power U_A and the AE index: $U_A(W) = 10^8 \times AE$ (nT). *Ahn et al.* [1983] compared the injected energy to the auroral geomagnetic indices and also obtained an empirical linear relation for the AE index, given by:

$$U_A(W) = 0.6 \times 10^8 \times AE \text{ (nT)}. \quad (2)$$

On the other hand, *Ostgaard et al.* [2002] proposed a nonlinear relation between the electron energy deposition and the geomagnetic indices, due to the saturation of the polar cap potential for large AE values

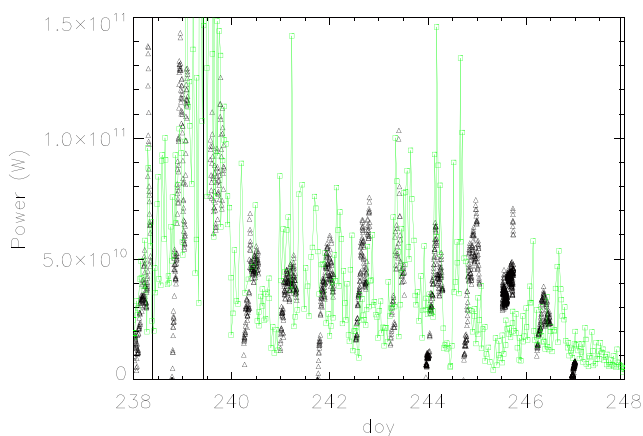


Figure 13. UVI total power over the entire polar region from 50° to 90° (black triangles) and the HP (green squares) during the LRP event of 26 August to 3 September 1998, Event 6.

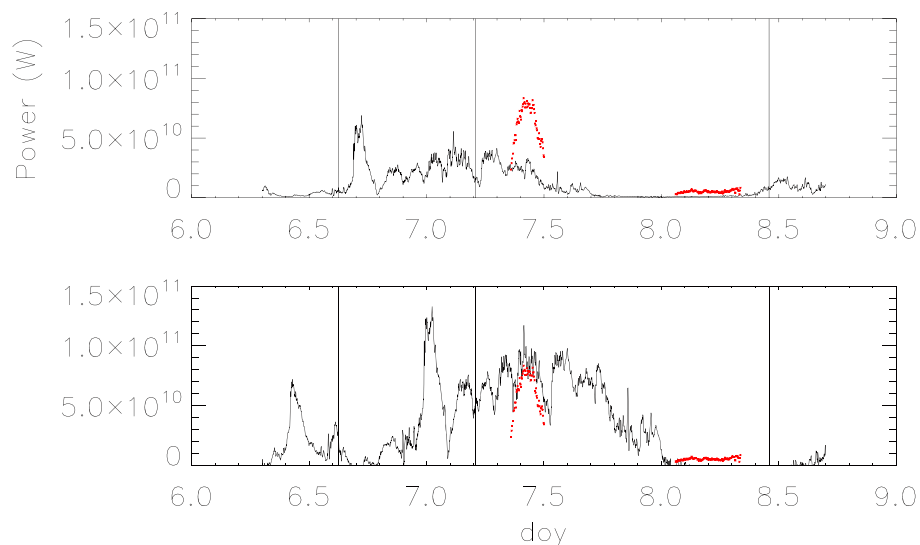


Figure 14. Power estimated from the UVI images (red) and the power calculated from the AE index (black) using the (top) linear equation (2) and (bottom) nonlinear equation (3) for the SRP Event 1.

[Lopez et al., 2010]. Comparing the precipitating particle energy estimated from the UVI and the X-ray emissions, they obtained the relation:

$$U_A(\text{GW}) = 4.6AE^{0.5}(\text{nT}) - 23(\text{GW}), \tag{3}$$

where the constant -23 GW indicates that there are still currents flowing when there is no precipitation.

We have calculated the power deposited by electrons in the auroral region using the linear empirical relation in equation (2) and the nonlinear in equation (3). Figures 14 and 15 show the power in black calculated from the AE index, where the linear relation was used for the top panel and the nonlinear equation for the bottom panel during the SRP (Event 1) and the LRP (Event 4) events, respectively. We compare the AE index power to the UVI total power plotted in red, previously described in section 4.1.

The UVI power for the SRP event seems to be closer to the nonlinear empirical power estimate, as seen in Figure 14 (bottom). The Events 2 and 3 exhibit roughly the same behavior as the Event 1, mainly during

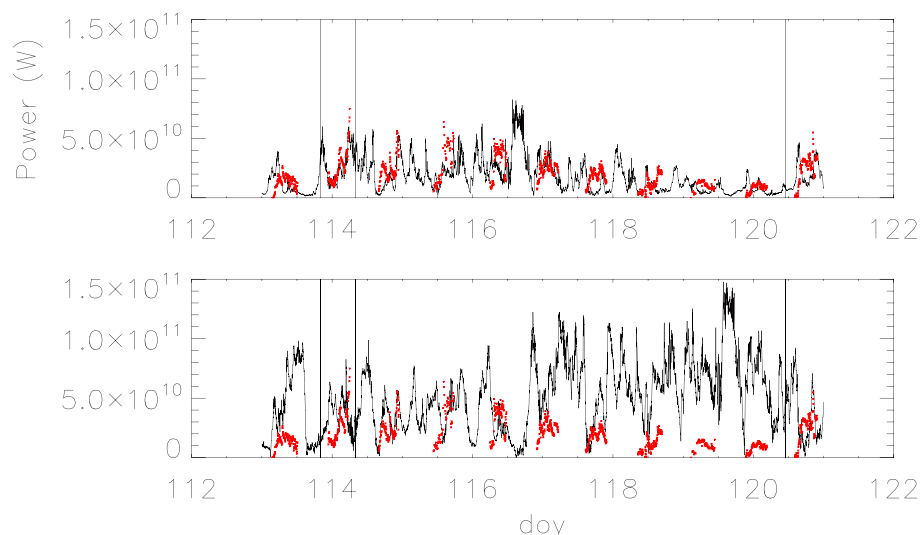


Figure 15. Power estimated from the UVI images (red) and the power calculated from the AE index (black) using the (top) linear equation (2) and (bottom) nonlinear equation (3) for the LRP Event 4.

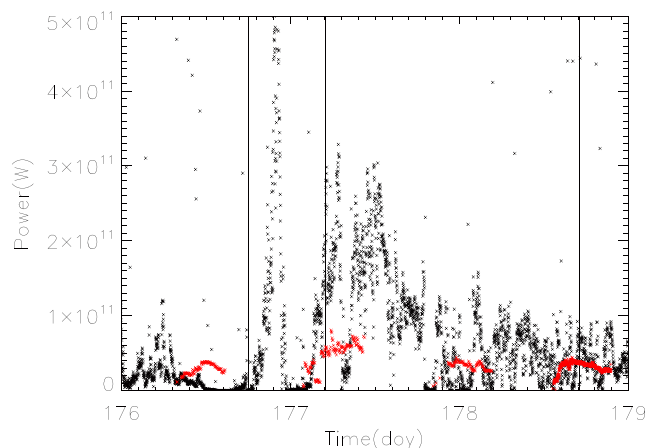


Figure 16. UVI electron precipitating (red) and solar wind input power from equation (4) (black) for the SRP Event 3.

the recovery phase [Cardoso, 2010]. These results indicate that the AE index may have saturated during the SRP storms.

On the other hand, the power obtained from the linear relation fits well to the UVI power during the LRP Event 4, as shown in Figure 15 (top). The Events 5 and 6 also present the same features as Event 4 (see pages 67 to 72 in Cardoso [2010] for the plots). The power from the nonlinear equation overestimates the UVI power as seen in Figure 15 (bottom), suggesting that the AE index is not saturated for LRP storms. The UVI and the linear power estimate similarities suggest that the precipitating electron energy input enhancement affects directly the auroral

electrojets during LRP events. It is important to notice that the quasiperiodic variation observed for the AE index empirical power during the LRP events in Figure 15 has also been found in the UVI power and in the HP.

4.3. UVI Estimate and Solar Wind Power Input

We have previously investigated the energy transfer processes between particle injection and the magnetospheric current systems. However, besides studying the energy transfer mechanisms inside the magnetosphere, it is essential to look at the major process driving the different magnetospheric phenomena. The coupling between the solar wind and the Earth magnetic field is believed to be responsible for the large amount of injected energy into the magnetosphere. This solar wind energy input is then mostly converted into particle precipitation in the auroral region, Joule heating, and ring current enhancement [Akasofu, 1981; Ostgaard et al., 2002].

The ϵ parameter indicates the energy input quantity in the solar wind responsible for the energy transfer to the magnetosphere [Perreault and Akasofu, 1978; Akasofu, 1981]. This parameter depends on the solar wind speed v , the IMF magnitude B , the clock angle θ (angle defined between the north Earth magnetic field component and the IMF in the GSM coordinate system) and the effective cross-sectional area l_0^2 , and is defined in SI units by

$$\epsilon(W) = \frac{4\pi}{\mu_0} v B^2 \sin^4(\theta/2) l_0^2. \quad (4)$$

The ϵ parameter is basically derived from Poynting's theorem [Koskinen and Tanskanen, 2002]. The factor $4\pi v B^2 / \mu_0$ corresponds to 4π times the Poynting vector magnitude calculated from upstream solar wind quantities and assuming that the magnetic field is perpendicular to the velocity. The electric field E is given by vB , from the assumption that the conductivity approaches infinity, which is valid for the solar wind.

The parameter l_0^2 in equation (4) is attributed to the effective cross-sectional area of the energy transfer [Akasofu, 1981]. Koskinen and Tanskanen [2002] claim that such factor with physical dimension of length is used for numerically scaling ϵ to correspond to the dissipated energy inside the magnetosphere and to satisfy the physical dimension of power. Estimated at $7 R_E$, l_0 is assumed to not strongly depend on the solar wind quantities and corresponds to the average dayside magnetopause distance.

The strong dependence of ϵ on the clock angle is addressed with the IMF north-south component. The factor $\sin^4(\theta/2)$ varies from 1 to 0 as the angle changes from 180° to 0° which yields larger amount of energy input for southward IMF values.

We compare the power for the solar wind input and the UVI total power to investigate the role of the solar wind energy transfer to the auroral dissipation energy. The solar wind power calculated from equation (4) (black) and the UVI power (red) are shown in Figures 16 and 17, for the SRP Event 3 and for the LRP Event 4, respectively. The solar wind data were obtained by the ACE spacecraft.

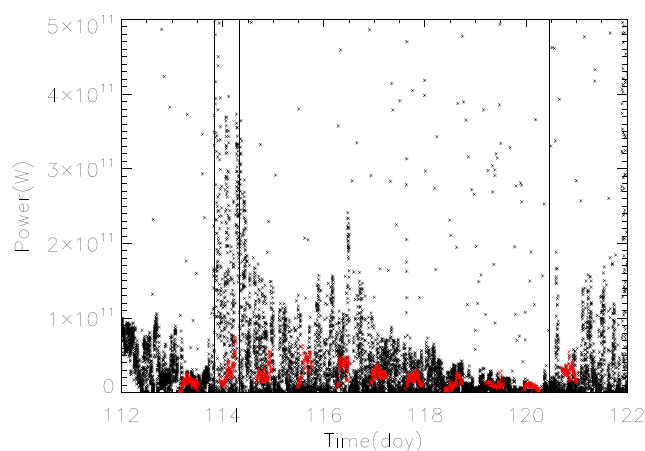


Figure 17. UVI electron precipitating (red) and solar wind input power from equation (4) (black) for the LRP Event 4.

coupling and dissipation. The energy supply coming from the solar wind kinetic energy may be above 10 TW, while the power penetrating the entire magnetosphere would be of the order of 1 TW and the level of the power dissipated into the storm and the substorm processes would be at the magnitude of about 100 GW. We have obtained the solar wind power input larger than 100 GW indicating that there is enough energy for triggering storms and substorms during the studied events.

The same fluctuation behavior seen in the UVI power for the LRP events can be observed for the solar wind input power for the Event 4 in Figure 17 and also in the Events 5 and 6 (for plots, see pages 85 to 86 in *Cardoso [2010]*). For all the LRP events, the maximum of the solar wind power is reached during the main phase and the energy spikes are decreasing in intensity as the recovery phase comes to an end.

Akasofu [1981] claims that if the magnetosphere is assumed to initially store solar wind energy and afterward converts the stored energy into substorm or magnetic storm energy, the relationship between ϵ and the dissipated energy would certainly not be simple. This system is the so-called loading-unloading system. On the other hand, if the ϵ parameter correlates well, for instance, with the precipitating power, the magnetosphere would not be a loading-unloading system but a driven system. According to this idea, SRP magnetic storms could be an effect of a loading-unloading system, since there is no clear relation between the UVI estimate and the solar wind input ϵ for Event 2 (see page 84 in *Cardoso [2010]* for the plot) and Event 3 (Figure 16). The Event 1 presented a large lack of data. The LRP events, which are associated with HILDCAAs, follow the fluctuations observed in the solar wind power and could be related to the driven system mechanism.

5. Final Remarks

The main goal in this work has been to estimate quantitatively the energy deposition by electron precipitation in the auroral region during magnetic storms presenting short and long recovery phases. The SRP is a characteristic of an ordinary magnetic storm. The LRP events are, sometimes, associated with HILDCAAs, which are characterized by producing high- and long-term auroral activity. We have presented the UVI estimate, the auroral power HP, the auroral dissipated power from the AE index and the solar wind power input for the selected events. The comparison between the energy estimate during the SRP and the LRP events may be an important issue, since there are many unanswered questions and scarce quantitative studies on the HILDCAA energy [*Hajra et al., 2014*].

The auroral precipitating energy has been derived from the LBH long emissions measured by the Polar UVI instrument. The UVI images have been treated by applying adjustment methods such as the spacecraft LOS corrections and the dayglow removal. We have developed a new dayglow estimate method which evaluates the dayglow energy and permits that the dayglow be removed from the UVI images. This procedure yields a quantitative analysis of the precipitating electron energy into the auroral region.

We have calculated the auroral energy flux for sectors of 10° ML and 3h MLT, and our results show the interesting feature of a quasiperiodic fluctuation for the LRP events. Mostly, the UVI energy flux presented higher

In the main phase of the storm, the solar wind power reaches a maximum of 500 GW for the SRP event (Figure 16) and about 375 GW for the LRP event (Figure 17). According to *Akasofu [1981]*, input power exceeding 100 GW can be considered enough energy for a substorm to occur and should be above 1 TW for magnetic storms. *Koskinen and Tanskanen [2002]* showed that the ϵ parameter should be considered as a first approximation for the solar wind-magnetosphere energy coupling.

After a discussion on the ϵ parameter, *Koskinen and Tanskanen [2002]* came up with a global picture of the energy

values at the nightside and near dusk for both types of events, but the LRP events last longer and reach larger energy values than the SRP events.

The UVI power has also been calculated for the entire auroral region. However, the UVI field of view changes during the spacecraft track and the varying area may affect the power estimate. For this reason, we selected the UVI images covering more than 60% of the auroral region to avoid any area variability influence. We observed in the UVI total power the same fluctuation pattern found for the LRP events in the UVI sectors estimate. The space-based auroral estimates of HP confirmed the quasiperiodic behavior for the LRP events. Moreover, we noticed the same fluctuating feature for the auroral dissipated power obtained from the *AE* index and for the solar wind input power ϵ during the LRP storms.

The comparison between the UVI total power and the HP estimate showed that the power peaks roughly around the *Dst* minimum, which indicates that the maximum of the ring current enhancement occurs simultaneously with the maximum of precipitating electron power in the auroral region during the analyzed SRP and the LRP events. The maximum of the ϵ parameter, representing the solar wind power, is reached during the magnetic storm main phase. The solar wind power spikes decrease in intensity as the recovery phase comes to an end, suggesting that the available energy in the solar wind follows the pattern seen in the magnetic storm phases defined by the *Dst* index.

We have compared the power deposited by electrons in the auroral region calculated from the *AE* index and the UVI total power. The *AE* index power has been computed using the linear (equation (2)) and the nonlinear (equation (3)) empirical relations. The UVI power for the SRP events seems to approach the nonlinear empirical power estimates, indicating that there may be saturation of the *AE* index during these events. On the other hand, the UVI power during the LRP events is closer to the *AE* index power obtained from the linear relation, suggesting that the precipitating electron energy input enhancement affects directly the auroral electrojets.

The solar wind input estimated from the ϵ parameter presented a good correlation with the UVI total power for the LRP events. According to Akasofu [1981], it indicates that the LRP magnetic storm may be a result of a directly driven system, and there is no long-term energy storage in the magnetosphere. On the other hand, there is no clear relation between the UVI power and the ϵ parameter obtained for the SRP events. In this case, the magnetosphere initially stores the solar wind energy and then converts it into substorm or magnetic storm energy. The mechanism involved in the SRP storm is called the loading-unloading system and we do not expect a simple relation between the ϵ and the dissipated auroral energy [Akasofu, 1981]. The comparison between the UVI total power and the power obtained from the *AE* index confirms our previous statements, since the auroral electrojets are directly affected by the electron precipitating power during the LRP events and there may be saturation of the *AE* index for the SRP storms.

The LRP magnetic storms are usually associated with HILDCAAs. According to Tsurutani and Gonzalez [1987], Alfvén waves have been detected during HILDCAAs, showing fluctuating magnetic field. The southward turnings of the IMF may be responsible for triggering reconnection processes at the magnetopause producing bursty particle injections into the magnetosphere. In fact, we have found the bursty features in the UVI power and in the ϵ parameter. Kim *et al.* [2008] showed that the large majority of repetitive particle injection during the HILDCAA events are associated with the substorm onsets. However, Lee *et al.* [2006] pointed out that the substorms are related to the successive northward turnings of Alfvén waves during the HILDCAA phenomena.

Acknowledgments

We are thankful for the Polar UVI data (<ftp://pwgdata.gsfc.nasa.gov/pub/compressed/po/uv/>), for the *AE* and *Dst* indices from the World Data Center for Geomagnetism at Kyoto, (<http://wdc.kugi.kyoto-u.ac.jp/aedir/index.html>), for the ACE solar wind data (<http://www.srl.caltech.edu/ACE/ASC>), and for the solar irradiance data from FISM (<http://lasp.colorado.edu/lisird/fism>). The UVI power for the studied events and the daylight estimate are available from the authors. F.R. Cardoso would like to thank grants 454672/2014-4 from the National Council for Scientific and Technological Development of Brazil (CNPq) and 2015/21376-4 from São Paulo Research Foundation (FAPESP). F.J.R. Simões Jr. would like to thank CNPq (Brazil), grant 473931/2013-3. D. Koga would like to thank the CNPq grant 112886/2015-9. M.V. Alves would like to thank the CNPq grant 305373/2010-2. We are grateful to Barbara Emery and the anonymous reviewer for their helpful comments.

References

- Ahn, B., S. Akasofu, and Y. Kamide (1983), The joule heating production and the particle energy injection rate as a function of the geomagnetic indices *AE* and *AL*, *J. Geophys. Res.*, *88*(A8), 6275–6287.
- Akasofu, S.-I. (1981), Energy coupling between the solar wind and the magnetosphere, *Space Sci. Rev.*, *28*(2), 121–190.
- Cardoso, F. R. (2010), Auroral electron precipitating energy during magnetic storms with peculiar long recovery phase features, PhD thesis in Space Geophysics, INPE-National Institute for Space Research, Sao José dos Campos, Brazil. [Available at <http://urlib.net/8JMKD3MGP7W/38HLGUE>.]
- Chamberlin, P., T. Woods, and F. Eparvier (2007), Flare irradiance spectral model (FISM): Daily component algorithms and results, *Space Weather*, *5*, S07005, doi:10.1029/2007SW000316.
- Chamberlin, P., T. Woods, and F. Eparvier (2008), Flare irradiance spectral model (FISM): Flare component algorithms and results, *Space Weather*, *6*, S05001, doi:10.1029/2007SW000372.
- Chua, D., G. Parks, M. Brittnacher, G. Germany, and J. Spann (2004), Auroral substorm timescales: IMF and seasonal variations, *J. Geophys. Res.*, *109*, A03207, doi:10.1029/2003JA009951.
- Emery, B. A., D. S. Evans, M. S. Greer, E. Holesman, K. Kadinsky-Cade, F. J. Rich, and W. Xu (2006), The low energy auroral electron and ion hemispheric power after NOAA and DMSP intersatellite adjustments, *NCAR Sci. and Tech. Rep. NCAR/TN-470+STR*, p. 76, NCAR, Boulder, Colo. [Available at <http://nldr.library.ucar.edu/repository/collections/TECH-NOTE-000-000-000-834-for.pdf>.] download under 'Full Text'.

- Emery, B. A., V. Coumans, D. S. Evans, G. A. Germany, M. S. Greer, E. Holeman, K. Kadinsky-Cade, F. J. Rich, and W. Xu (2008), Seasonal, K_p , solar wind, and solar flux variations in long-term single pass satellite estimates of electron and ion auroral hemispheric power, *J. Geophys. Res.*, *113*, A06311, doi:10.1029/2007JA012866.
- Fillingim, M., G. Parks, L. Chen, M. Brittnacher, G. Germany, J. Spann, D. Larson, and R. Lin (2000), Coincident POLAR/UVI and WIND observations of pseudobreakups, *Geophys. Res. Lett.*, *27*(9), 1379–1382.
- Fillingim, M., G. Parks, L. Chen, M. McCarthy, J. Spann, and R. Lin (2001), Comparison of plasma sheet dynamics during pseudobreakups and expansive aurorae, *Phys. Plasmas*, *8*(4), 1127–1132.
- Fillingim, M., G. Parks, H. Frey, T. Immel, and S. Mende (2005), Hemispheric asymmetry of the afternoon electron aurora, *Geophys. Res. Lett.*, *32*, L03113, doi:10.1029/2004GL021635.
- Germany, G. A., M. R. Torr, P. G. Richards, and D. G. Torr (1990), The dependence of modeled OI 1356 and N₂ Lyman Birge Hopfield auroral emissions on the neutral atmosphere, *J. Geophys. Res.*, *95*(A6), 7725–7733.
- Germany, G. A., M. R. Torr, D. G. Torr, and P. G. Richards (1994), Use of FUV auroral emissions as diagnostic indicators, *J. Geophys. Res.*, *99*(A1), 383–388.
- Germany, G. A., J. F. Spann, G. K. Parks, M. J. Brittnacher, R. Elsen, L. Chen, D. Lummerzheim, and M. H. Rees (1998), Auroral observations from the Polar Ultraviolet Imager (UVI), in *Geospace Mass and Energy Flow*, *Geophys. Monogr. Ser.*, edited by J. L. Horwitz, D. L. Gallagher, and W. K. Peterson, pp. 149–160, AGU, Washington D. C.
- Gonzalez, W. (1990), A unified view of solar-wind magnetosphere coupling functions, *Planet. Space Sci.*, *38*(5), 627–632.
- Guarnieri, F., B. T. Tsurutani, E. Echer, and W. Gonzalez (2007), Geomagnetic activity and auroras caused by high-speed streams: A review, in *Advances in Geosciences: Solar Terrestrial*, vol. 8, edited by M. Duldig et al., pp. 91–102, World Sci., Singapore.
- Hajra, R., E. Echer, B. T. Tsurutani, and W. Gonzalez (2014), Solar wind-magnetosphere energy coupling efficiency and partitioning: HILDCAAS and preceding CIR storms during solar cycle 23, *J. Geophys. Res. Space Physics*, *119*, 2675–2690, doi:10.1002/2013JA019646.
- Kim, H.-J., D. Lee, and L. Lyons (2008), Are repetitive particle injections during high-speed solar wind streams classic substorms?, *J. Geophys. Res.*, *113*, A08205, doi:10.1029/2007JA012847.
- Koskinen, H. E., and E. I. Tanskanen (2002), Magnetospheric energy budget and the epsilon parameter, *J. Geophys. Res.*, *107*(A11), 1415, doi:10.1029/2002JA009283.
- Lee, D.-Y., L. Lyons, K. Kim, K.-H. K. J.-H. Baek, H.-J. Kim, J. Weygand, Y. Moon, K.-S. Cho, Y. Park, and W. Han (2006), Repetitive substorms caused by Alfvénic waves of the interplanetary magnetic field during high-speed solar streams, *J. Geophys. Res.*, *111*, A12214, doi:10.1029/2006JA011685.
- Liou, K., P. Newell, and C.-I. Meng (2001), Seasonal effects on auroral particle acceleration and precipitation, *J. Geophys. Res.*, *106*(A4), 5531–5542.
- Lopez, R., R. Bruntz, E. Mitchell, M. Wiltberger, J. Lyon, and V. Merkin (2010), Role of magnetosheath force balance in regulating the dayside reconnection potential, *J. Geophys. Res.*, *115*, A12216, doi:10.1029/2009JA014597.
- Lummerzheim, D., M. Brittnacher, D. Evans, G. Germany, G. Parks, M. Rees, and J. Spann (1997), High time resolution study of the hemispheric power carried by electrons into the ionosphere during the May 19/20, 1996 auroral activity, *Geophys. Res. Lett.*, *24*(8), 987–990.
- Meier, R. R. (1991), Ultraviolet spectroscopy and remote sensing of the upper atmosphere, *Space Sci. Rev.*, *58*(1), 1–185.
- Ostgaard, N., R. R. Vondrak, J. W. Gjerloev, and G. Germany (2002), A relation between the energy deposition by electron precipitation and geomagnetic indices during substorms, *J. Geophys. Res.*, *107*(A9), 1246, doi:10.1029/2001JA002003.
- Palmroth, M., P. Janhunen, G. Germany, D. Lummerzheim, K. Liou, D. N. Baker, C. Barth, A. T. Weatherwax, and J. Watermann (2006), Precipitation and total power consumption in the ionosphere: Global MHD simulation results compared with Polar and SNOE observations, *Ann. Geophys.*, *24*, 861–872.
- Perreault, P., and S. Akasofu (1978), Study of geomagnetic storms, *Geophys. J. R. Astron. Soc.*, *54*(3), 547–573.
- Torr, M. R., D. G. Torr, M. Zucic, R. B. Johnson, J. Ajello, P. Banks, K. Clark, K. Cole, C. Keffer, G. Parks, B. Tsurutani, and J. Spann (1995), A far ultraviolet imager for the international solar terrestrial physics mission, *Planet. Space Sci.*, *71*, 329–383.
- Tsurutani, B. T., and W. D. Gonzalez (1987), The cause of High-Intensity Long Duration AE Activity (HILDCAAS): Interplanetary Alfvén wave trains, *Planet. Space Sci.*, *35*(4), 405–412.